University of Nevada, Reno

# Optical Characterization of Fresh and Photochemically-Aged Aerosols Emitted from Laboratory Siberian Peat Burning

A thesis submitted in partial fulfillment of the
requirements for the degree of Master of Science
in Atmospheric Science

By

Michealene M. M. Iaukea-Lum

Dr. Hans Moosmüller/Thesis Advisor

December 2018

THE GRADUATE SCHOOL

We recommend that the thesis
prepared under our supervision by

**MICHEALENE IAUKEA-LUM**

Entitled

**Optical Characterization Of Fresh And Photochemically-Aged Aerosols Emitted From Laboratory Siberian Peat Burning**

be accepted in partial fulfillment of the
requirements for the degree of

MASTER OF SCIENCE

Hans Moosmuller, Ph.D., Advisor

Eric Wilcox, Ph.D., Committee Member

Patrick Arnott, Ph.D., Graduate School Representative

David W. Zeh, Ph.D., Dean, Graduate School

December, 2018

## Abstract

Carbonaceous aerosols emitted from biomass burning into the atmosphere greatly influences radiative forcing and climate change on regional and global scales. Of particular interest are emissions from high latitude peat burning because of the large amount of terrestrial carbon stored in peatlands and becoming increasingly susceptible to wildfires due to amplified climate change at high latitude. Here, we have combusted small amounts of Siberian Peat in a laboratory biomass-burning facility. We have characterized the optical properties of freshly-emitted and photochemically-aged combustion aerosols, including absorption and scattering coefficients, at three wavelengths, 405, 532, and 781nm. The atmospheric aging of emitted aerosols was simulated using an Oxidation Flow Reactor (OFR) at timescales equivalent to three weeks to two months of atmospheric aging. Siberian peat was used as fuel because of its slow and smoldering combustion and its common importance in high-latitude peatland fires. Our results show that freshly emitted aerosols cause light extinction including scattering and absorption and while this extinction is modified during atmospheric aging, scattering and absorption can continue for weeks to months after the burn event until the aerosol is deposited on the earth surface; therefore emitted aerosols can continue to alter the radiation budget on these timescales.Our measurements on Siberian peat biomass burn emissions showed an increase in particle number density during aging. However, total particle volume either increased or decreased, depending on the aging duration. Measured scattering and absorption coefficients and their sum, the extinction coefficient, were used to calculate aerosol single-scattering albedo (SSA) as ratio of scattering and extinction coefficients, SSA is the dominant intensive aerosol optics parameter determining aerosol radiative forcing. Our data analysis showed that SSA of both fresh and aged aerosol increased with increasing wavelength; this is expected for brown carbon (BrC) aerosols. Changes in SSA between freshly emitted and aged aerosols were greatest at the 405 nm wavelength where SSA values increased by ~2% after aging. This SSA increase was likely dominated by a decrease

in absorption coefficient instead of by an increase in scattering coefficient. SSA changes at the 532 and 781 nm wavelengths were less obvious and were easier to observe in terms of co-albedo. Single scattering co-albedo values showed aged emissions became more absorbent than fresh emissions at 532 nm by 32% and at 781 nm became less absorbent by ~16% indicating a shift in absorption toward longer wavelengths and a decrease in Absorption Ångström exponent (AAE). Although these percentages may seem significant, they refer to values whose magnitudes are of the order of $10^{-3}$. Absorption Ångström exponents ranged from ~6 to 9 denoting much stronger absorption at shorter wavelengths, both before and after aging. The extraction of the complex refractive index yielded real parts that increased with increasing wavelength which is unusual for wavelengths well above the wavelengths of the dominant absorption features. The imaginary part of the complex refractive index decreased with increasing wavelength as expected. For all three wavelengths (405, 532, and 781nm), the values of the real part of the complex refractive index ranged from 1.3 to 1.6 for aged emissions and 1.3 to 1.8 for fresh ones while imaginary parts of the complex refractive index were in the range of 0.0002 to 0.0096 for aged emissions and 0.0002 to 0.0175 for fresh ones. These values are typical for brown carbon aerosols from biomass combustion.

Table of Contents

List of Tables

List of Figures

## Introduction

Biomass-burning emissions dominate carbonaceous aerosol mass emissions into the atmosphere on a global scale (Bond et al., 2004), greatly contributing to radiative forcing and climate change (IPCC et al., 2013), visibility impairment (Watson, 2002), effects on human health (Pope III and Dockery, 2006), ecosystem processes (Niyogi et al., 2004), and agricultural productivity (Tie et al., 2016). Many of these processes are driven by the optical properties of the emitted aerosols, therefore creating much interest in optical properties of biomass burning emissions and their change during atmospheric processing. While there has been extensive work on optical properties of freshly emitted biomass burning aerosols (e.g., Chakrabarty et al., 2010, 2016; Chen et al., 2006, 2007; Cheng et al., 2016; Levin et al., 2010; Samburova et al., 2016) much less is known about the change of their optical properties during atmospheric processing (Liousse et al., 1995; Popovicheva et al., 2016). These changes are induced by multiple processes including (1) the generation of secondary organic aerosols (SOAs; (Hennigan et al., 2011; Ortega et al., 2013)), (2) particle coagulation (Radke et al., 1995), (3) condensation and evaporation of volatile compounds (Jolleys et al., 2015), (4) modification of black carbon (BC) aggregates (Mishchenko et al., 2016), and (5) chemical transformations that either produce or destroy brown carbon (BrC; (Saleh et al., 2013)).

In the laboratory, atmospheric aging can be simulated either in a smog chamber or an oxidation flow reactor (OFR). Traditional smog chambers age emissions over time periods comparable to those in the atmosphere (e.g., hours to days), while OFRs age emissions much more rapidly using very high oxidant (e.g., OH and $O_3$) concentrations (Bruns et al., 2015) produced by intense ultraviolet radiation. Yields and composition of resulting, aged emissions can agree between smog chambers and OFRs within measurement uncertainties, thereby supporting the use of OFRs to efficiently study atmospheric aging of biomass burning emissions (Bruns et al., 2015).

In terms of fuels, we combusted Siberian peat as an important example fuel from northern peatlands, which represent an estimated carbon (C) reservoir of ~ 547 Gt C (Yu, 2012). Drying of peatlands as a result of climate change and human activities makes these carbon stocks more susceptible to fires (Turetsky et al., 2015) and increases the need for characterization of combustion emissions and their atmospheric transformations.

Here, we study three-wavelength absorption and scattering coefficients of biomass burning aerosols from the combustion of Siberian peat, freshly emitted by small-scale laboratory combustion of biomass and after atmospheric aging simulated in an OFR.

## 1 Experiment

### 1.1 Overview

Small samples of Siberian peat (~50 g) were combusted in the DRI biomass-burning facility and alternatingly fresh and OFR-aged emissions were characterized with real time instrumentation and filter sampling followed by laboratory analysis. A diagram of this experimental setup is shown in Fig. 1 and a more in-depth explanation and characterization of this setup has been given by Bhattarai et al. (2018). Such laboratory experiments can help evaluating the direct radiative forcing of biomass burning emissions by determining aerosol scattering and absorption coefficients of laboratory emissions. The OFR was operated at three lamp voltages corresponding to different UV actinic fluxes to simulate the aging of particles in the atmosphere on the order of days, weeks, and months (Bhattarai et al., 2018).

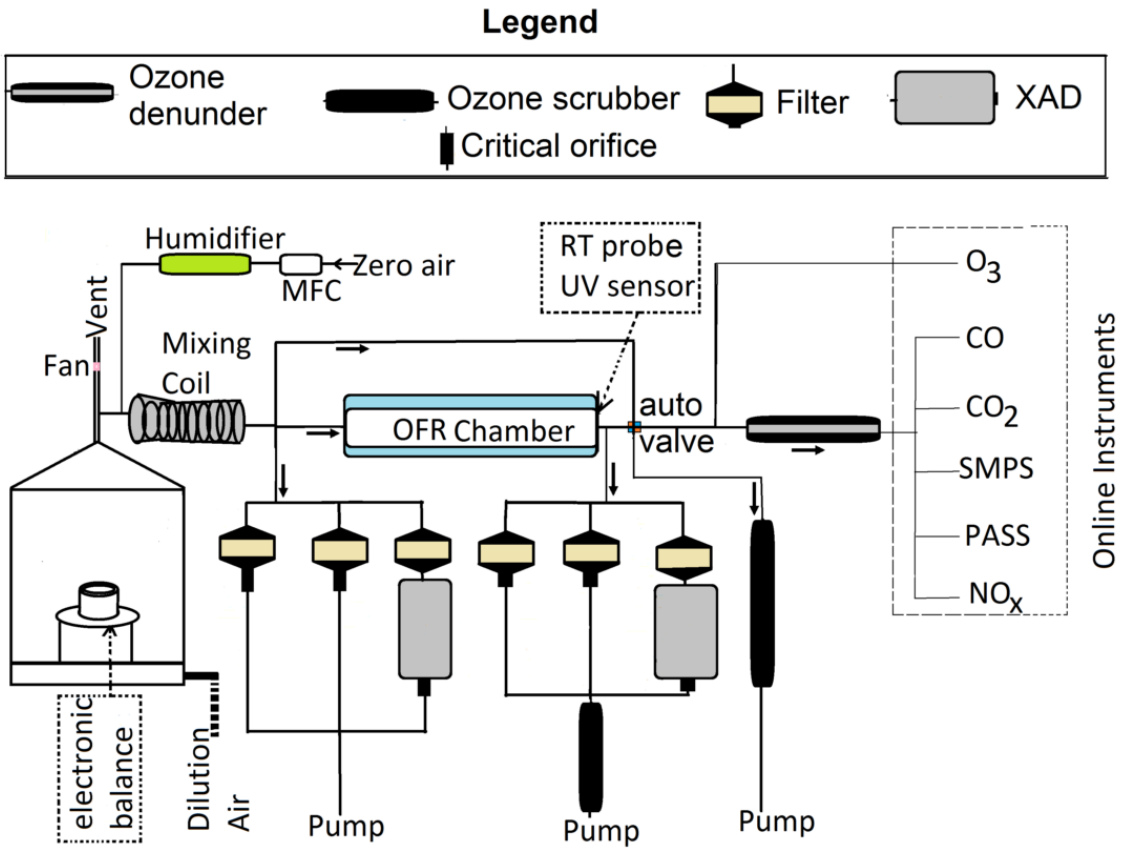


**Figure 1: Experimental setup for generating, aging, and characterizing biomass burning aerosols as previously described by Bhattarai et al. (2018)**.

Instruments used for the characterization of fresh and aged biomass burning emissions included Droplet Measurement Technologies (DMT) Three Wavelength Photoacoustic Soot Spectrometer (PASS-3), Aerodyne Inc. Oxidation flow reactor (OFR), 2B Technologies Inc. ozone monitor (Model 205), and a scanning mobility particle sizer (SMPS) comprised of a TSI 3080 Electrostatic Classifier and a TSI 3775 Condensation Particle Counter (CPC). Aerosol emissions were also sampled on Teflon and quartz filters for laboratory analysis. CO, $CO_2$, and $NO_X$ concentrations were measured with a CO monitor [Model 8830 CO analyser, LEAR Siegler Measurement Controls Corporation], a Li-7000 $CO_2/H_2O$ Analyzer [LICOR Biosciences], and a chemiluminescence $NO_X$ analyser [Model 42 Thermo – Environmental Instruments Inc.] respectively. Individual components of the experimental setup are described in more detail in the following subsections.

**1.2 DRI Biomass-Burning Facility**

The DRI biomass-burning facility consists of a laboratory chamber constructed from aluminum panels enclosing a square base (1.83 m × 1.83 m) and is 2.06 m high. Above this height, the chamber tapers to an exhaust pipe that contains multiple sampling ports and exhausts chamber air to a roof outlet with the exhaust flow rate controlled by a fan and a variable opening for the air inlet located at the bottom of the chamber, directly below the burn platform (Samburova et al., 2016). A close replica of this facility has been described by Tian et al. (2015). Small amounts (~50 g) of fuel were burned in this chamber under controlled conditions (relative humidity, temperature, fuel-moisture content, etc.). The fuel weights during the burns were monitored every second with a Veritas L Series Precision balance (0.01 g of precision). The resulting aerosol emissions were sampled from the chamber exhaust through a primary sampling line into a sampling manifold that split the flow to multiple sample lines. Sample lines, made of non-reactive conductive polytetrafluoroethylene (PTFE) tubing, were connected to real-time instruments and medium volume filter/XAD samplers. Optical characterization of biomass-burning emissions was performed with a three-wavelength photoacoustic spectrometer and nephelometer (PASS-3, Droplet Measurement Technologies, Boulder, CO, USA; (Arnott et al., 1999; Lewis et al., 2008; Moosmüller et al., 2009a)

**1.3 Biomass Burning Fuel**

Siberian peat was used as fuel due to its regional and global importance as wildland fuel and due to its steady smoldering combustion. In addition, peat is utilized on a widespread scale in homes and industry as a fuel source for energy production including heating and cooking applications. It is found in the wild as decaying wetland vegetation, and due to the very large carbon pool storage in peat lands (Yu et al., 2011), the smoldering combustion of drained or dried out peat beds can result in very large emissions of carbonaceous gases (e.g., $CO_2$ and CO) and carbonaceous aerosols and their precursors. In addition, the drying out of peatlands is becoming more common

due to climate change and human activities, therefore making peatlands more susceptible to fires (Turetsky et al., 2015) and consequently increasing the need for characterizing peat combustion emissions and their atmospheric transformations. Peat found in European Russia in the region of Pskov was used in our experiment. Siberia and Pskov, Russia share common ecosystems with vegetation comprised of Sphagnum and cotton grass (Eriphorum spp.). We identify our fuel as Siberian peat because of the much more extensive peat lands in Siberia that are comprised of the same species as our samples from the Pskov region (Sengupta et al., 2018).

**1.4 Oxidation Flow Reactor (OFR)**

During biomass burns the sampling flow for the real time instruments was switched at ten-minute intervals between fresh chamber flow - bypassing the OFR - and aged chamber flow - ducted through the OFR. The OFR creates OH radicals through an accelerated process simulating photodissociation which naturally occurs over the course of several days (Lambe et al., 2011). This process is controlled using UV-lamps operated at given voltages, located inside the reactor chamber, which act as a source of artificial light. Four UV-lamps (two at 185 nm and two at 254 nm wavelengths) were utilized inside the flow reactor for the production of ozone and OH radicals (Bhattarai et al., 2018). The presence of the OH radical is key to the development of secondary aerosols because of its reactive nature, quickly oxidizing pollutants (Cody et al., 1991). Table 1 shows the parameters under which the OFR was operated during our laboratory experiments.

**Table 1: UV irradiance, temperature, ozone, CO, and water concentration, and calculated equivalent age in the ORF. Values in brackets represent standard deviation of the measurements.**

| | Measurement | | | | | |
|---|---|---|---|---|---|---|
| Operation Voltage (V) | UV intensity ($\mu W\ cm^{-2}$) | T (°C) | $O_3$ (ppm) | CO (ppm) | Water ($mg/m^3$) | Age (days) |
| 3 | 229.9 | 28.0 (0.1) | 17.3 (0.2) | 33.98 (0.02) | 11.81 (0.02) | 19.3 (0.3) |
| 5 | 503.6 | 31.5 (0.3) | 26.4 (0.3) | 20.96 (0.03) | 12.03 (0.05) | 44.1 (0.6) |
| 7 | 688.9 | 33.5 (0.2) | 32.8 (0.3) | 15.07 (0.02) | 12.03 (0.03) | 61.1 (0.6) |

**1.5 Photoacoustic Soot Spectrometer (PASS-3)**

The Photoacoustic Soot Spectrometer (PASS-3; Droplet Measurement Technologies, Inc.) primarily measures aerosol absorption coefficients through the photoacoustic effect and simultaneously, aerosol scattering coefficients with a reciprocal nephelometer, both in the same sample volume and at the three operating wavelengths (405, 532, and 780 nm) (Moosmüller et al., 2009b). Photoacoustic measurements of absorption coefficients of aerosols in their natural, suspended state are considered a primary standard with an error of ~5%, while the simultaneous measurements of scattering coefficients have an error of ~15% (Abu-Rahmah et al., 2006; Gyawali et al., 2017; Moosmüller and Arnott, 2003). Measurements of absorption and scattering coefficients at three wavelengths allows for the calculation of aerosol single scattering albedo (SSA), and single scattering co-albedo (SSCA) at three wavelengths. It also allows for calculation of the single scattering co-albedo Ångström exponent (SSCAAE), absorption Ångström exponent (AAE), scattering Ångström exponent (SAE), and extinction Ångström exponent (EAE) between pairs of two operating wavelengths or, through linear regression over the three operating wavelengths (Moosmüller and Chakrabarty, 2011).

**1. 6 Scanning Mobility Particle Sizer (SMPS, TSI)**

The Scanning Mobility Particle Sizer (SMPS) was comprised of two instruments: (1) a TSI 3080 Electrostatic Classifier selecting a size bin and (2) a TSI 3775 Condensation Particle Counter (CPC) counting the number of particles in the size bin selected by the classifier. This pairing of instruments allowed for submicrometer particles to be sized with high resolution from 16.5 to 988 nm (Bhattarai et al., 2018; TSI INC, 2001).

As sample air entered the SMPS at a flow rate of 0.3 LPM, particles were initially preselected by aerodynamic size with an inlet impactor. With the help of sheath flow, larger particles (>1000 nm in aerodynamic diameter) are removed from the sample air and expelled through the excess

air port while smaller particles (diameters 2 nm to 1000 nm) move past the inlet impactor. After this pre-selection, particles were charged to a known charge distribution by an aerosol charge neutralizer (TSI Kr-85), before entering the differential mobility analyser (DMA) to be size selected. Sheath flow in the DMA region of the SMPS remained at a constant 3.0 L/min during all sampling periods. After a particle size bin was selected by the DMA, particles in this size bin were counted by the CPC. This counting is achieved by introducing butanol ($C_4H_9OH$) vapor into the sample stream and consequently cooling the sample stream, resulting in a large supersaturation of the butanol vapor. Condensation readily occurs with the particles serving as condensation nuclei, quickly growing to a size that can be detected with an optical scattering detector, thereby enabling the counting of particles larger than 4 nm in diameter.

The TSI software used to process the data assumes a pressure differential of one atmosphere (1 atm). This means that the output data did not account for the change in pressure caused by the elevation at which the instrument was operated. As a result, a correction was made to the SMPS data that addressed this issue.

**2 Experiments and Data Sets**

Biomass burning emissions were drawn from the burn chamber through the PASS – 3 and other online instruments using an external pump (Fig. 1). A more detailed explanation of the sampling can be found in Bhattarai et al. (2018). PASS-3 measurements of absorption and scattering coefficients were performed with two-second time resolution. Raw data were filtered and down-averaged to a time resolution of ten seconds before analysis. Further data analysis was performed to obtain insight on effects such as determining whether or not absorption values were influenced by the presence of ozone in the sample flow and to retrieve the complex refractive indices of the particles, which required the particle size distribution in addition to absorption and scattering coefficients.

**2.1 PASS-3 Data Sets**

The experimental setup (Fig. 1) used an automated valve to alternate every 10 minutes between fresh and aged samples. Switching caused a pressure fluctuation in the sample volume of the PASS-3 resulting in temporary data artifacts. Additional artifacts were created during the automatic zero calibration of the PASS-3 that was performed every 20 minutes. Therefore, data affected by sample alternation and zero calibration artifacts were omitted from the analysis. For every timed valve switch and each zero calibration two minutes of data were removed. After this initial filtering there was an average of seven minutes of valid data for each ten-minute interval of fresh or aged sampling.

Each Siberian peat sample smoldered for ~50 minutes, yielding an average of ~1050 data points for each burn. A ten second averaging was performed allowing for more manageable data sets without compromising their information content. The ten second averaged data also allowed for direct comparison with the ten second data output of the ozone monitor.

Due to the high ozone concentrations generated by the OFR (see Table 1), ozone absorption in the Chappuis band (Brion et al., 1998) can result in artifacts for photoacoustic measurements of aerosol absorption coefficients (Yu et al., 2017). Therefore, our experimental setup included an ozone denuder before the PASS-3 (Fig. 1) and an ozone monitor was used to measure ozone concentrations past this denuder. Results indicated that absorption by ozone at the PASS-3 wavelengths was miniscule (<<1% of the measured aerosol absorption) and could be neglected for our study.

**2.2 SMPS Data Sets**

Data from the SMPS was processed using software that did not consider the elevation at which the instrument was operated assuming an operating environment at sea level with ambient pressure of 1 atm during sampling. During our experiments, the SMPS was operated at an

elevation of ~1,516 m ASL, corresponding to an ambient pressure of ~0.83 atm. Therefore, a pressure correction code was run on the SMPS output that exported the data as

$$f = \frac{dN}{d \log D_p}, \tag{1}$$

where $f$ is the size distribution function, $N$ is the number concentration, and $D_p$ is the particle diameter bin size. In order to find the number concentration, N, after running the Python pressure correction code, the output was divided by 192, the number of bins. More information on this correction can be found in subsection 4.1: Particle Size Distribution.

## 3 Data Analysis

In our experiment, peat samples burned nearly exclusively in smoldering combustion, which produced near-spherical organic carbon particles also known as tar balls (Chakrabarty et al., 2010). Therefore, Mie theory can be used conveniently to analyze aerosol optical properties. Optical properties that can be calculated using the scattering and absorption coefficients measured by the PASS – 3, alongside the particle size distribution measured by the SMPS include single scattering albedo (SSA), absorption, scattering, and extinction Ångström exponents (AAE, SAE, and EAE), and the complex refractive indices.

### 3.1 Single Scattering Albedo

The single scattering albedo (SSA) is used to describe the "whiteness" of aerosol particles with its maximum value of one corresponding to pure scattering (no absorption) and its minimum value of zero corresponding to pure absorption (no scattering). SSA can be mathematically defined as the ratio between the scattering $\beta_{sca}$ and extinction $\beta_{ext}$ coefficients

$$SSA = \frac{\beta_{sca}}{\beta_{ext}} = \frac{\beta_{sca}}{\beta_{sca} + \beta_{abs}}, \tag{2}$$

where the extinction coefficient is the sum of the scattering and absorption coefficients. For homogeneous spherical particles, SSA is only a function of the particle complex refractive index and size parameter (i.e., the ratio of particle circumference and wavelength) (Moosmüller and Arnott, 2009; Moosmüller and Sorensen, 2018). SSA can be calculated directly with Eq. (2) from PASS-3 measurements of scattering and absorption coefficients either through individual ratios (Eq. (2)) or from the slope of a linear regression between absorption and scattering coefficients (Moosmüller et al., 2012) as

$$SSA = (1 + \frac{1}{slope^{-1}})^{-1}. \quad (3)$$

**3.2 Ångström Exponent**

Besides the SSA, the Ångström exponent AE is another critical parameter used to describe and evaluate aerosol radiative forcing in the atmosphere (Pokhrel et al., 2016). The AE is a power law exponent approximately describing the wavelength dependence of scattering, absorption, and extinction coefficients (yielding SAE, AAE, and EAE, respectively) as

$$\frac{\beta_{\lambda_1}}{\beta_{\lambda_2}} = \left(\frac{\lambda_1}{\lambda_2}\right)^{-AE}, \quad (4)$$

where $\beta_\lambda$ is the scattering, absorption, or extinction coefficient at wavelength $\lambda$ and the Ångström (SAE, AAE, or EAE) exponent can be written as

$$AE = \frac{\ln(\beta_{\lambda_1}) - \ln(\beta_{\lambda_2})}{\ln(\lambda_2) - \ln(\lambda_1)}. \quad (5)$$

**3.3 Complex Refractive Index**

The complex index of refraction is an intensive material property that determines the interaction of light with a medium. For spherical particles emitted by smoldering combustion, their optical

properties depend solely on their complex refractive index $m = n + i\kappa$ and their size parameter $x$, defined as the ratio of particle circumference $\pi d$ and the wavelength of the incident light λ with

$$x = \frac{\pi d}{\lambda}, \tag{6}$$

where $d$ is the particle diameter.

While the forward problem of calculating optical properties from the complex refractive index and the size parameter is straightforward using Mie theory, the inverse problem of retrieving the complex refractive index from optical and size measurements is not straightforward. Recently, the PyMieScatt computational package written in Python has become available (Sumlin et al., 2018a); it contains a very robust inversion package for retrieval of the complex refractive index, which has been used here. Input parameters for the PyMieScatt inversion are the scattering and absorption coefficients directly measured with the PASS-3, the particle size distribution determined with the SMPS, and the three wavelengths used for the PASS-3 optical measurements.

**3.4 Error Propagation**

In a scattering versus absorption plots, the slope of the resulting regression line can be used to calculate the single scattering albedo (SSA) for a given wavelength as shown in Eq. (3). In a linear regression plot of scattering between two different wavelengths, the slope of the regression can be used to calculate the Ångström exponent (AE) as shown in Eq. (5). In both methods, an ideal regression line should pass through the origin. However, this is not always the case for real data.

During our experiments some regression lines did not pass through the origin as ideally expected and instead intersected the vertical axis slightly above or below the origin (±100 to 1000 $Mm^{-1}$). As a result, two sets of calculated SSA and AE were generated. The first set used the raw slopes

and a second set of values used slopes with regression lines forced through the origin. The two sets of slopes differed at most by $10^{-2}$. This difference between slopes remained the same for SSA, AAE, SAE, and EAE slopes. A t-Test with Paired Two Sample for Means was used to determine if there was a significant difference between the two sets of calculated SSA and AE values. Results showed that there was no significant difference between these two versions. Therefore, all regression lines were forced through the origin and all SSA and AE values were calculated using the resulting slopes.

Further calculations were performed to characterize error propagation from the mean between individual data points and the regression line found in (Taylor, 1997). Deviation from the mean for single scattering albedo and for Ångström exponents were found to be in the ranges from 0.00004 to 0.0173, and from 0.0015 to 0.33, respectively.

## 4 Results and Discussion

### 4.1 Particle Size Distribution

During our experiments, we measured scattering and absorption coefficients at three different wavelengths (405, 532, and 781 nm) and characterized the particle size distributions over the measurement range of our SMPS (i.e., 16.5 to 988 nm). These combinations of wavelengths and particle diameters yield size parameters ranging from 0.128 to 7.66 at 405 nm, from 0.097 to 5.83 at 532 nm, and from 0.066 to 3.97 at 781 nm.

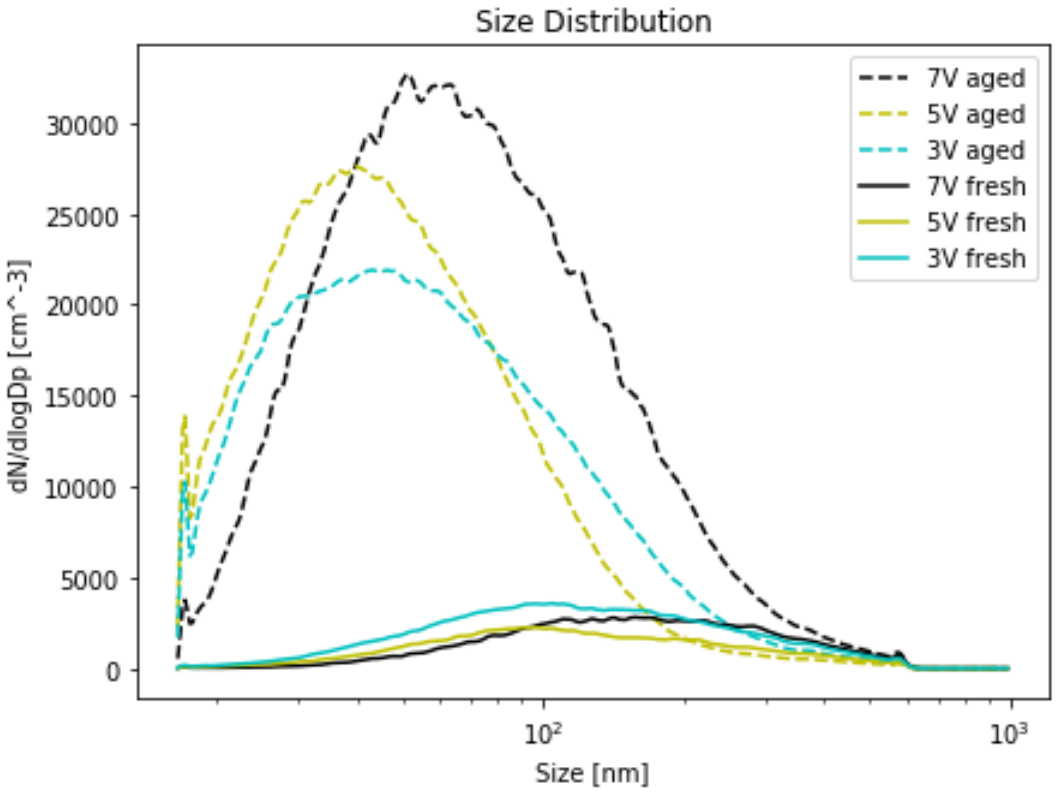


**Figure 2: Particle size distribution for aerosols emitted from the combustion of Siberian Peat.**

The SMPS output normally puts size distributions into bins per decade and for our setup, there were 64 bins per decade. During the pressure correction, the SMPS resolution was increased to 192 bins per decade. Therefore, the data shown in Fig. 2 represents the pressure corrected size distribution with 192 bins per decade.

Particle counts increased when fresh emissions were aged in the OFR due to particle generation. When comparing particle number concentrations between fresh to aged, particle counts increased by ~1020% at UV-lamp operating voltage of 7V, equivalent to 61 days of aging. At 5V (44 days) particle counts increased by ~957%, and at 3V (19 days) by ~506%.

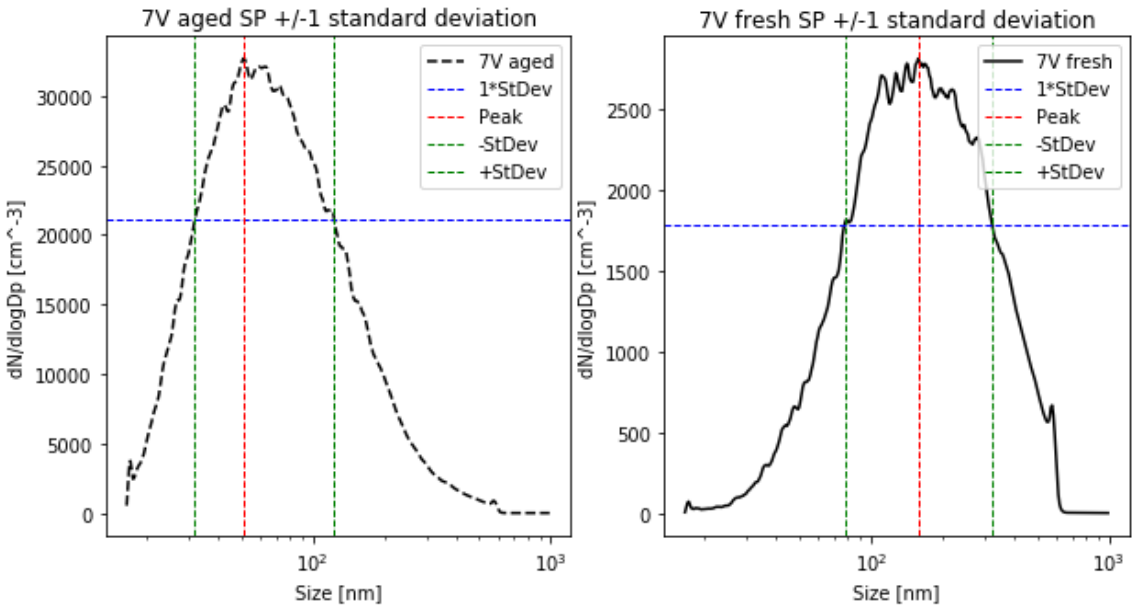


**Figure 3: Particle distributions with standard deviations for Siberian peat (SP) combustion emissions. Left: aged (61 days). Right: fresh.**

There was an increase in particle count when emissions were aged in the OFR, and there also was a shift in peak particle size. Emissions altered between fresh and 19 days of aging displayed a shift in size range from 58 nm – 234 nm during fresh sampling to 22 nm – 105 nm during aged sampling. These values were taken ± one standard deviation from the peak of the distribution (Fig.3). For all OFR operating voltages (3V, 5V, and 7V), particle size ranges decreased switching from fresh to aged Siberian peat biomass burn emissions. Our results show that while total particle count increased during aging, size range decreased by ~50%. This could possibly be due to both evaporation reducing large particle sizes and due to nucleation of small particles during aging. The shift in size range and particle counts is also documented in Table 2, which gives numerical values for the significant parameters from Fig. 3 for three OFR operating voltages and aging times.

**Table 2: Standard deviations of particle counts for Siberian peat emissions for aging and fresh.**

| Voltage | Aged or Fresh | Avg Particle Count | Peak | St. Dev. | Peak - St. Dev. | Size Range [nm] |
|---|---|---|---|---|---|---|
| 3V (19 days) | Aged | 9783 | 21903 | 8269 | 13634 | 22 - 105 |
| | Fresh | 1615 | 3566 | 1229 | 2337 | 58 - 234 |
| 5V (44 days) | Aged | 10168 | 27585 | 10157 | 17427 | 23 - 79 |
| | Fresh | 962 | 2237 | 735 | 1502 | 59 - 218 |
| 7V (61 days) | Aged | 13445 | 32663 | 11559 | 21104 | 32 - 123 |
| | Fresh | 1200 | 2812 | 1028 | 1784 | 78 - 324 |

Total particle volume gives the sum of the particle volume per bin for each burn. For spherical particles, the volume of an individual particle can be written as

$$V_{sphere} = \frac{4}{3}\pi * r^3, \quad (7)$$

where r is the particle radius. Multiplying the individual particle volume with the particle count for each size bin and summing these "bin" volumes over all bins yields the total particle volume emitted per burn. When comparing fresh to aged total particle volume, there was significant difference between the two for each OFR operating voltage (Table 3).

The total particle volume of aged emissions increased from fresh by ~1.89% when aged at an OFR operating voltage of 3V (19 days), decreased by ~7.24% when aged at a voltage of 5V (44 days) and showed a very large increase in total particle volume of ~88.02% when aged at 7V (61 days).

**Table 3: Total particle volume for each OFR operating voltage with fresh and aged Siberian peat emissions.**

| Total Particle Volume | | | |
|---|---|---|---|
| Voltage | Fresh [$nm^3$] | Aged [$nm^3$] | % inc or dec |
| 3V | 3.23E+12 | 3.29E+12 | +1.89 |
| 5V | 1.96E+12 | 1.82E+12 | -7.24 |
| 7V | 3.63E+12 | 6.83E+12 | +88.02 |

This large variation in total particle volume could possibly be due to the type of particles generated after aging. Although the count for aged particles is 500% to 1000% greater than that of fresh emission counts, these particles are mostly smaller in size as shown in Table 2. So, if the number of large particles decreases or if larger particles partly evaporate during aging, it is possible for total particle volume emissions to decrease due to aging as did happen at 5V (44 days) in Table 3. However, if net particle mass is generated during aging, possibly due to new particle generation and growth and growth of existing particles, the total particle volume of the aged emissions will outgrow the fresh as it did at 7V (61 days) in Table 3. Here the fresh particles were larger, but fewer in count by one order of magnitude. Once aged, the sum of the smaller volumes overpowered the sum of the fresh volumes causing an increase in total particle volume by ~88.02%. To determine the voltage thresholds between particle volume increase and decrease will require additional experiments and analysis.

**4.2 Single Scattering Albedo**

The particle single scattering albedo (SSA) is the dominant intensive aerosol optics parameter determining aerosol radiative forcing (Chylek and Wong, 1995; Hassan et al., 2015). SSA is generally wavelength dependent and can range from zero for completely absorbing particles with no scattering to one for completely scattering particles with no absorption. Results from our laboratory biomass burns show an increase in single scattering albedo with increasing wavelength, meaning that with increasing wavelength, scattering coefficients decrease slower than absorption coefficients (Moosmüller and Chakrabarty, 2011). Aging our combustion emissions in the OFR by days (3V), weeks (5V), and months (7V), changed the SSA values at the three wavelengths of observation, 405, 532, and 781 nm. Absorption coefficients values changed by $10^1$ $Mm^{-1}$ to $10^3$ $Mm^{-1}$ when moving from 405 to 532 to 781 nm. However, when comparing changes of SSA between fresh and aged biomass burn emissions, changes in the absorption coefficients were overcome by changes in the scattering coefficients that ranged in order of $10^5$

$Mm^{-1}$ to $10^6$ $Mm^{-1}$ both before and after aging of biomass burn emissions. This resulted in changes in single scattering albedo being driven by the scattering coefficients.

Table 4 and Fig. 4 display these SSA values with accompanying uncertainty values ranging from ± 0.00005 to ± 0.00422 for fresh emissions and ± 0.00018 to ± 0.0173 for aged emissions.

**Table 4: Single scattering albedo at three wavelengths for fresh and aged aerosols.**

| Aging | Wavelength (nm) | Slope aged | Slope fresh | SSA aged | SSA fresh |
|---|---|---|---|---|---|
| 3V (19 days) | 405 | 17.7 | 14.3 | 0.947±0.000822 | 0.935±0.00422 |
| | 532 | 111.3 | 116.7 | 0.991±0.000470 | 0.992±0.000483 |
| | 781 | 513.3 | 588.6 | 0.998±0.000576 | 0.998±6.959E-05 |
| 5V (44 days) | 405 | 15.5 | 11.1 | 0.939±0.00668 | 0.917±0.00597 |
| | 532 | 98.4 | 115.5 | 0.989±0.00102 | 0.991±0.000809 |
| | 781 | 1027.9 | 697.9 | 0.999±0.000269 | 0.999±0.000126 |
| 7V (61 days) | 405 | 15.4 | 14.6 | 0.939±0.0173 | 0.936±0.00156 |
| | 532 | 85.6 | 143.5 | 0.988±0.00434 | 0.993±9.937E-05 |
| | 781 | 737.4 | 1263.7 | 0.999±0.000182 | 0.999±4.846E-05 |

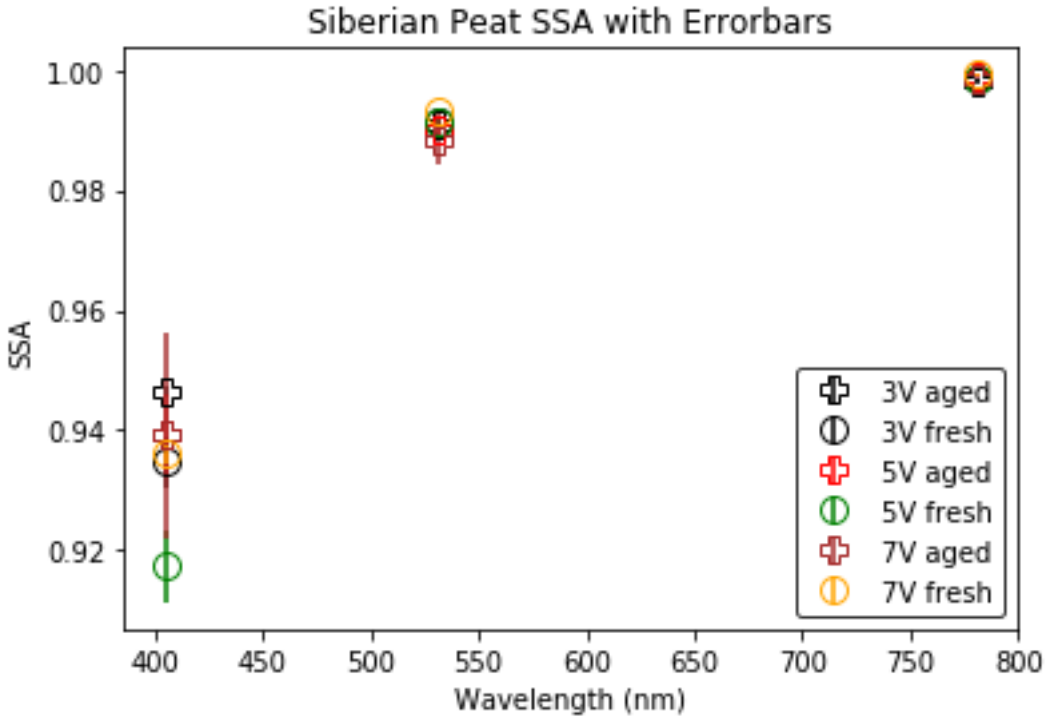


**Figure 4: SSA with error bars as function of wavelength for fresh and aged aerosols.**

Looking specifically at the 405, 532, and 781 nm SSA, SSA at the shorter wavelength of 405 nm was affected more by aging than at the other two wavelengths. In Fig. 4 there is a distinct separation of the aged (plus) and the fresh (circle) with the aged emissions having increased SSA. This could be caused by a bleaching (decreasing of absorption) due to UV or OH exposure in the OFR.

The 405 nm wavelength showed the greatest change in SSA during transition from fresh to aged aerosols. The SSA increased by 0.022 during OFR operation at 5V (weeks); the largest change in SSA observed during our experiments. This is equivalent to a 2% increase in SSA most likely due to a decrease in absorption. The next largest SSA increase of 0.012 was again at 405 nm with an OFR operation of 3V (days), and the third largest increase occurred at 405 nm of 0.003 during OFR operation of 7V (months). We hypothesize that during aging, SSA is initially strongly increased due to generation of additional BrC and then gradually decreases due to bleaching of chromophores.

The longer wavelengths of 532 and 781 nm showed smaller changes in SSA values from fresh to aged in which some increased and others decreased. To gain a better perspective on the behavior of SSA at these longer wavelengths, we examine the single scattering co-albedo (SSCA) of the aerosols.

SSCA is defined as 1 - SSA, and can be described as the fraction of extinction due to absorption, and can be written as,

$$SSCA = 1 - SSA = \frac{\beta_{abs}}{\beta_{ext}}. \quad (8)$$

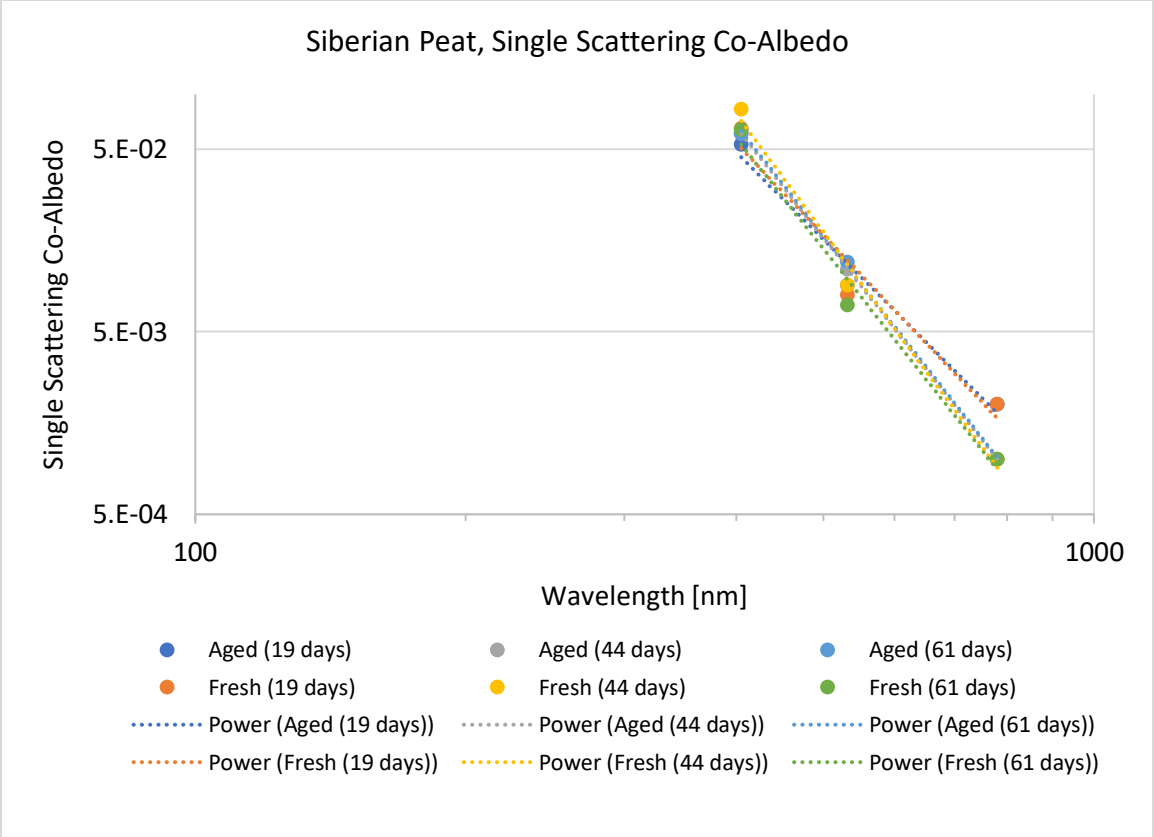


**Figure 5: A log-log plot of single scattering co-albedo (SSCA) as function of wavelength for fresh and aged Siberian peat biomass burn emissions.**

By plotting the SSCA as a function of wavelength on a log-log scale, it becomes possible to better visualize SSA changes at the longer wavelengths of 532 and 781 nm, and to determine if SSCA wavelength dependence follows a simple power law indicated by an approximately straight line with an Ångström exponent equaling the negative slope (Moosmüller et al., 2011). Fitting a power-law to the measurements, the negative exponents represent the single scattering co-albedo Ångström exponent (SSCA AE). Table 5 shows the associated SSCA AE and their $R^2$ values. Correlation coefficients $R^2$ are in the range of 0.954722 to 0.99999800, indicating an excellent linear fit in log-log space with the power laws giving an excellent approximation of the observed values.

**Table 5: SSCA AE and R2 values for aged and fresh emissions.**

| | Single Scattering Co-Albedo Ångström Exponents (SSCA AE) | | | |
|---|---|---|---|---|
| Voltage | SSCA AE Aged | SSCA AE Fresh | $R^2$ Value Aged | $R^2$ Value Fresh |
| 3V | 4.92 | 5.19 | 0.979183 | 0.95472 |
| 5V | 6.26 | 6.66 | 0.999998 | 0.98991 |
| 7V | 6.27 | 6.25 | 0.999488 | 0.98202 |

Co-albedo values at 405 nm are highest of the three observed wavelengths representing the greater absorption by brown carbon at shorter wavelength corresponding to smaller SSA values. The co-albedo values for fresh/aged wavelengths of 532 and 781 nm were lower than 405 nm (less absorbing) and range from 0.007-0.009/0.009-0.012 and 0.00087-0.00207/0.00073-0.00127 respectively. At the 532 nm wavelength co-albedos of aged aerosols were 22-25% higher than those of fresh aerosols and at 781 nm they were 16-39% lower than those of fresh aerosols. A graphical representation of co-albedo values can be seen in Fig. 5.

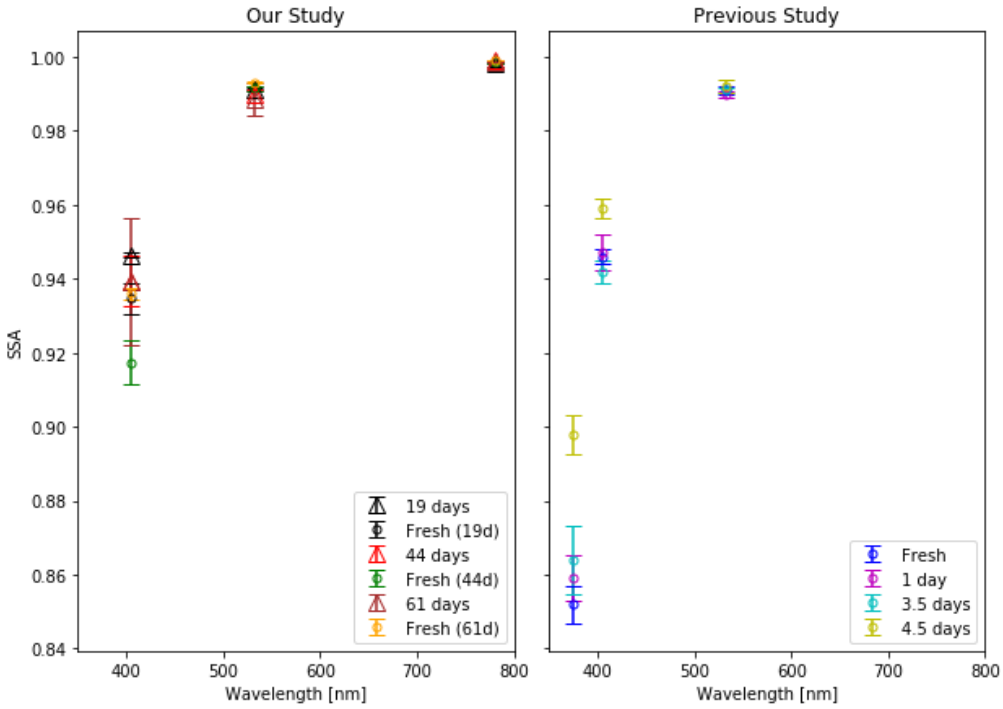


**Figure 6: Fresh and aged single scattering albedo with associated error bars. Left: our results. Right: previously published results by Sumlin et al., (2018b) for aerosols emitted from Alaskan peat combustion.**

Figure 6 shows SSA values with associated error bars for laboratory-derived data. On the right-hand side are the results from a previous laboratory biomass burning study by Sumlin et al. (2018b) that observed the aging of emissions from combustion of densely packed Alaskan peat retrieved near Tok, Alaska. This study used wavelengths of 375, 405, 532, and 1047 nm and aging times included fresh, one day, 3.5 days, and 4.5 days of aging. For the purpose of comparison to our results, SSA values from aged emissions of fuels with a moisture content of 20% have been plotted in Fig. 6 (right panel). Similar to our results, Sumlin et al. (2018b) also observed a small increase in SSA near 0.99 at the 532 nm wavelength. Our results also show increasing SSA with increasing wavelength with SSA very close to one at wavelengths of 532 nm and greater.

**4.3 Absorption Ångström Exponent (AAE)**

Absorption Ångström exponents (AAEs) of ~1 are typically due to small (i.e., size parameter $x<<1$ or $d << \lambda$) black carbon (BC) particles (Moosmüller et al., 2009a; Srinivas and Sarin, 2014). In our experiments AAE values for the 405 - 532 nm wavelength range from ~8.5 - 9 for fresh aerosol samples and ~7.0 - 7.75 for aged samples. This shows a decrease in the AAE by 12 – 17% due to aging of emissions in the OFR. These values, which are much larger than 1, demonstrate that particle optics is dominated by BrC and not by BC particles as is expected for smoldering combustion (e.g., (Chakrabarty et al., 2010)).

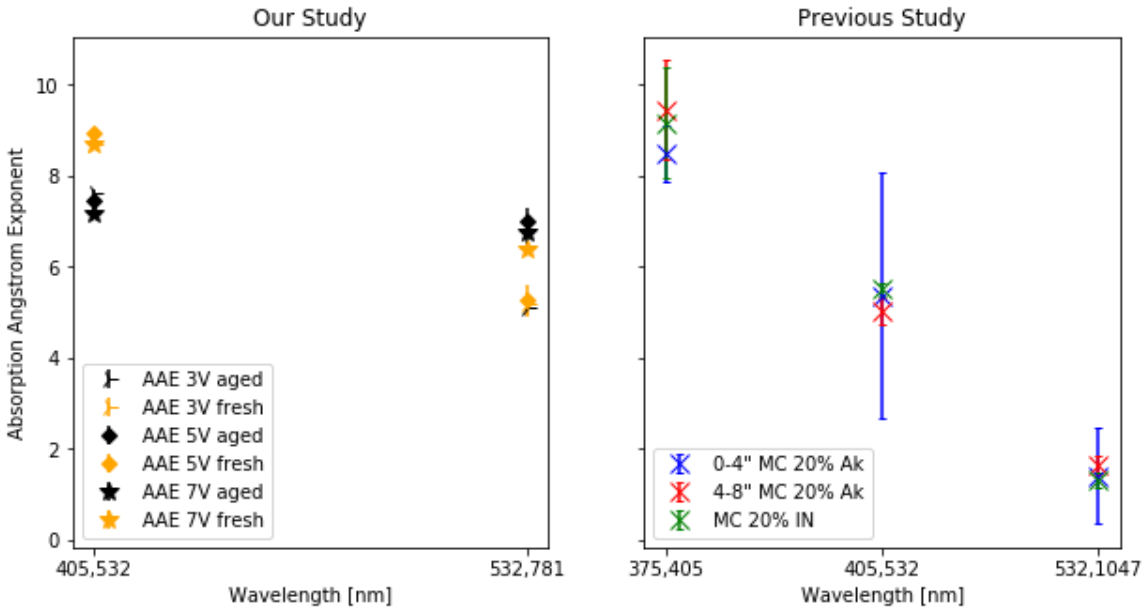


**Figure 7: Absorption Ångström exponent as function of wavelength pair. Left: this study. Right: previous study by Sumlin et al. (2018b).**

In a previous study performed by Sumlin et al. (2018b), similar results were observed in a laboratory setting. Their fuels included Alaskan peat (AK) and Indonesian peat (IN). When harvesting the AK fuel, the samples were extracted at different depths within the ground. These depths are represented at 0-4" and 4-8" in Fig. 7. Also, in order to compare our results to those of Sumlin et al. (2018b), only their results for peat with fuel moisture content (MC) of 20% are represented. Their samples were not densely packed, and their biomass burning emissions were not aged like ours, which may explain their difference of 2 – 3 in AAE at the 405,532 nm range. However, also notice the large error bars of Sumlin et al. (2018b) shown in Fig. 7 (right panel), making these differences barely significant.

**Table 6: Ångström exponents for absorption (AAE), scattering (SAE), and extinction (EAE) for emissions from Siberian peat combustion.**

| Aging | $\lambda$ (nm) | AAE aged | AAE fresh | SAE aged | SAE fresh | EAE aged | EAE fresh |
|---|---|---|---|---|---|---|---|
| 19 days (3V) | 405, 532 | 7.64 ± 0.061 | 8.69 ± 0.096 | 0.89 ± 0.050 | 0.49 ± 0.083 | 1.06 ± 0.048 | 0.75 ± 0.077 |
| | 532, 781 | 5.11 ± 0.099 | 5.18 ± 0.25 | 1.13 ± 0.066 | 0.95 ± 0.23 | 1.14 ± 0.066 | 0.97 ± 0.23 |
| | 405, 781 | 6.16 ± 0.089 | 6.64 ± 0.25 | 1.03 ± 0.11 | 0.76 ± 0.31 | 1.11 ± 0.11 | 0.88 ± 0.30 |
| 44 days (5V) | 405, 532 | 7.44 ± 0.089 | 8.93 ± 0.086 | 0.69 ± 0.052 | 0.34 ± 0.062 | 0.88 ± 0.044 | 0.63 ± 0.052 |
| | 532, 781 | 7.02 ± 0.26 | 5.29 ± 0.33 | 0.91 ± 0.070 | 0.61 ± 0.15 | 0.94 ± 0.069 | 0.63 ± 0.15 |
| | 405, 781 | 7.19 ± 0.29 | 6.8 ± 0.28 | 0.82 ± 0.12 | 0.49 ± 0.0015 | 0.92 ± 0.11 | 0.63 ± 0.19 |
| 61 days (7V) | 405, 532 | 7.18 ± 0.13 | 8.69 ± 0.033 | 0.89 ± 0.056 | 0.41 ± 0.078 | 1.08 ± 0.039 | 0.63 ± 0.073 |
| | 532, 781 | 6.78 ± 0.30 | 6.39 ± 0.13 | 1.18 ± 0.19 | 0.72 ± 0.12 | 1.21 ± 0.19 | 0.74 ± 0.12 |
| | 405, 781 | 6.95 ± 0.20 | 7.35 ± 0.12 | 1.06 ± 0.36 | 0.56 ± 0.15 | 1.16 ± 0.33 | 0.66 ± 0.15 |

Table 6 shows Ångström exponent values for absorption, scattering, and extinction calculated from our absorption and scattering coefficients using Eq. (6). Absorption Ångström exponents for fresh and aged emissions were within the 6 to 9 range denoting the dominance of strongly wavelength-dependent BrC absorption. Scattering Ångström exponents are much closer to one (1) indicating scattering dominated by scattering from large ($x >> 1$) particles. Because SSA is fairly close to one (1), extinction Ångström exponents are dominated by SAE values rather than by the much larger AAE values (Moosmüller and Chakrabarty, 2011). Notice also that changes in AAE between fresh to aged are not consistent with decreases in some cases and increases in others. Extinction Ångström exponents (EAE) are often utilized to determine if extinction is dominated by small particles (AE>2) or by large particles such as sea salt (AE<2); here it is clearly dominated by large particles and changes in EAE may be related to changes in particle size due to aging.

#### 4.4 Complex Refractive Index

Particle complex refractive indices were retrieved with the PyMieScatt open source package yielding complex refractive indices at the intersections of the scattering and absorption efficiency contours (Sumlin et al., 2018a). Scattering and absorption efficiencies and particle complex

refractive indices were calculated from the measured scattering and absorption coefficients, wavelengths of light, and the particle diameter size distribution data retrieved by the PASS-3 and SMPS, respectively. Results are similar to those of previous studies of aerosol emissions from combustion of peat fuels such as Alaskan and Indonesian peat (Sumlin et al., 2018b) and Florida peat (Sengupta et al., 2018).

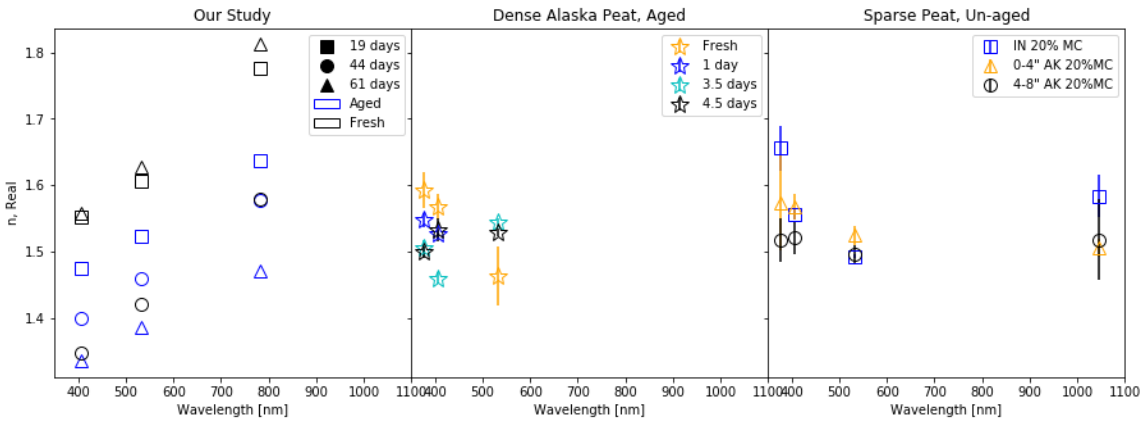


**Figure 8: Real part of the complex refractive index, n, vs wavelength. Left: our study, combustion emissions from Siberian peat. Center: combustion emissions from aged, densely packed Alaskan peat (Sumlin et al., 2018b). Right: non-aged combustion emissions.**

Figure 8 shows the real -parts of the particle refractive index. The left panel shows the results from our laboratory biomass burns of Siberian peat. The center and right panels show results from previous experiments by Sumlin et al. (2018 a or b). Again, comparisons were made with 20% MC for sparsely packed Indonesian and Alaskan peat and densely packed aged Alaskan peat. In contrast to Sumlin et al. (2018 a or b), our study extended the aging period of biomass burning aerosols beyond 4.5 days and into months (7V, 61 days). Notice the non-linear, increasing trend for the real part of the refractive index as a function of wavelength in Fig. 8 for our study. Previous studies did not demonstrate this trend.

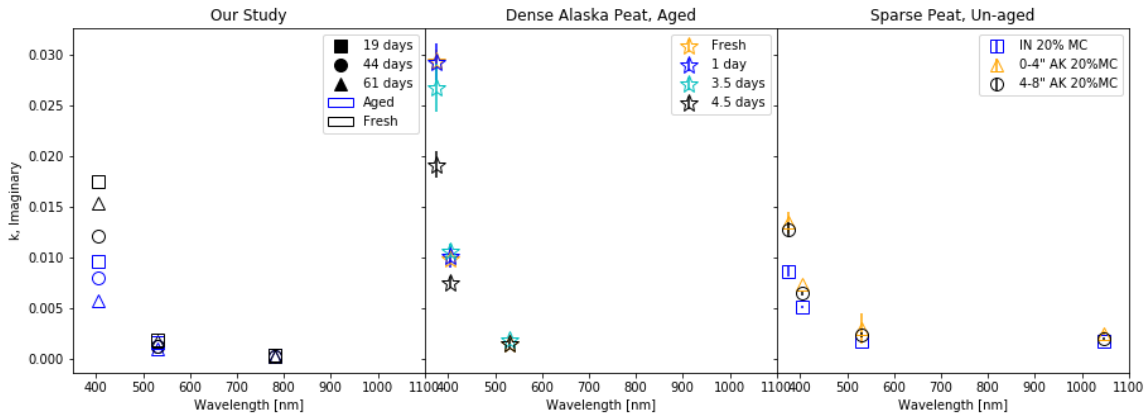


**Figure 9: Imaginary part of the complex refractive index, k, as function of wavelength. Left: our study, aged Siberian peat. Center: aged densely packed Alaskan peat. Right: non-aged sparsely packed Indonesian and Alaskan peat (Sumlin et al., 2018b).**

As the wavelength increases there is an inverse relation with the imaginary part of the complex refractive index, k, and a direct relation with the real part of the complex refractive index. The inverse relation of the imaginary part of the complex refractive index, k, to the wavelength is indicative of the presence of brown carbon aerosols where the absorption is strongly wavelength dependent. Our results reflected this reciprocal behavior of the imaginary part of the complex refractive index with respect to wavelength and can be see in Fig. 9.

The real part of the complex refractive index pertains mostly to scattering and the imaginary part mostly to absorption. For our study, results showed an increase in scattering properties linear with wavelength. The imaginary part of the complex refractive index, k, ranges from 0.0002 to $0.0096 \pm 0.001$ for aged emissions and 0.0002 to $0.0175 \pm 0.004$ for fresh emissions. Because the complex refractive index is strongly wavelength dependent, we deduce that the combustion emissions are not dominated by black carbon aerosols that have a largely wavelength-independent refractive index but by BrC.

## 5 Conclusion

Peatlands covers ~2% of the global land mass, and peatlands constitute the largest terrestrial carbon sink. As permafrost melts, more Siberian peatlands become susceptible to wildfires. Our study shows that emissions from biomass burning peatlands can have significant effects on surrounding environments. SSA values show not only strong scattering at the 532 and 781 nm wavelengths, but also strong absorption at the shorter wavelength of 405 nm, directly impacting the radiation budget and atmospheric photochemistry. Also, after aging of aerosols from the biomass burn, particle counts increase and depending on conditions can result in an increase in total particle volume. There is also an increase in the real part of the complex refractive index with wavelength. Our study investigated optical properties of aged Siberian peat biomass burning emissions with aging ranging from fresh to 19, 44, and 61 days. Previous studies have not studied this much aging and were limited to only ~4.5 days (Sumlin et al., 2018b). Through the extraction of the complex refractive index, we can conclude that the emissions from the Siberian peat biomass burn were dominated by the presence of brown carbon due to the attenuation of light being strongly wavelength dependent and scattering dominating absorption as indicated by relatively high SSA values.

## 6 Acknowledgments

Thank you, God. Thank you to my late mother, Sophia Iaukea, whose overwhelming love and support got me started and spurred me to finish in life and in death. A special thanks to my advisor Dr. Hans Moosmüller for never giving up on me. A very heartfelt thank you to Dr. Vera Samburova, Deep Sengupta, Dr. Patrick Arnott, and Dr. Eric Wilcox. A very big thank you to Ben Sumlin for being a cool guy and helping me from afar. Thank you to grants from NASA and NSF for financially supporting my endeavours. None of this would have been possible without

you. A final thanks to the couple who got me started in this field, Dr. James O. Juvik and Dr. Sonia Juvik, my hanai parents.

**References**

Abu-Rahmah, A., Arnott, W. P. and Moosmüller, H.: Integrating nephelometer with a low truncation angle and an extended calibration scheme, Meas. Sci. Technol., 17(7), 1723–1732, doi:10.1088/0957-0233/17/7/010, 2006.

Arnott, W. P., Moosmüller, H., Rogers, C. F., Jin, T. and Bruch, R.: Photoacoustic Spectrometer for Measuring Light Absorption by Aerosol: Instrument Description., Atmos. Environ., 33(17), 2845–2852 [online] Available from: https://hero.epa.gov/hero/index.cfm/reference/details/reference_id/20650, 1999.

Bhattarai, C., Samburova, V., Sengupta, D., Iaukea-Lum, M., Watts, A. C., Moosmüller, H. and Khlystov, A. Y.: Physical and chemical characterization of aerosol in fresh and aged emissions from open combustion of biomass fuels, Aerosol Sci. Technol., 52(11), 1266–1282, doi:10.1080/02786826.2018.1498585, 2018.

Bond, T. C., Streets, D. G., Yarber, K. F., Nelson, S. M., Woo, J.-H. and Klimont, Z.: A Technology-Based Global Inventory of Black and Organic Carbon Emissions from Combustion, J. Geophys. Res., 109(D14203), DOI:10.1029/2003JD003697, 2004.

Brion, J., Chakir, A., Charbonnier, J., Daumont, D., Parisse, C. and Malicet, J.: Absorption spectra measurements for the ozone molecule in the 350-830 nm region, J. Atmos. Chem., 30(2), 291–299, doi:10.1023/A:1006036924364, 1998.

Bruns, E. A., El Haddad, I., Keller, A., Klein, F., Kumar, N. K., Pieber, S. M., Corbin, J. C., Slowik, J. G., Brune, W. H., Baltensperger, U. and Prevot, A. S. H.: Inter-Comparison of Laboratory Smog Chamber and Flow Reactor Systems on Organic Aerosol Yield and Composition, Atmos. Meas. Tech., 8(6), 2315–2332, doi:10.5194/amt-8-2315-2015, 2015.

Chakrabarty, R. K., Moosmüller, H., Chen, L. W. A., Lewis, K., Arnott, W. P., Mazzoleni, C., Dubey, M. K., Wold, C. E., Hao, W. M. and Kreidenweis, S. M.: Brown carbon in tar balls from smoldering biomass combustion, Atmos. Chem. Phys., 10(13), 6363–6370, doi:10.5194/acp-10-6363-2010, 2010.

Chakrabarty, R. K., Gyawali, M., Yatavelli, R. L. N., Pandey, A., Watts, A. C., Knue, J., Chen, L. W. A., Pattison, R. R., Tsibart, A., Samburova, V. and Moosmüller, H.: Brown Carbon Aerosols from Burning of Boreal Peatlands: Microphysical Properties, Emission Factors, and Implications for Direct Radiative Forcing, Atmos. Chem. Phys., 16(5), 3033–3040, doi:10.5194/acp-16-3033-2016, 2016.

Chen, L.-W. A., Moosmüller, H., Arnott, W. P., Chow, J. C., Watson, J. G., Susott, R. A., Babbitt, R. E., Wold, C. E., Lincoln, E. N. and Hao, W. M.: Particle Emissions from Laboratory Combustion of Wildland Fuels: In Situ Optical and Mass Measurements, Geophys. Res. Lett., 33(L04803), doi:10.1029/2005GL024838, 2006.

Chen, L.-W. A., Moosmüller, H., Arnott, W. P., Chow, J. C., Watson, J. G., Susott, R. A., Babbitt, R. E., Wold, C. E., Lincoln, E. N. and Hao, W. M.: Emissions from Laboratory

Combustion of Wildland Fuels: Emission Factors and Source Profiles, Environ. Sci. Technol., 41(12), 4317–4325, 2007.

Cheng, Y., Engling, G., Moosmüller, H., Arnott, W. P., Chen, A. L. W., Wold, C. E. and Hao, W. M.: Light Absorption by Biomass Burning Source Emissions, Atmos. Environ., 127, 347–354, 2016.

Chylek, P. and Wong, J.: Effect of absorbing aerosols on global radiation budget, Geophys. Res. Lett., 22(8), 929–931, doi:10.1029/95GL00800, 1995.

Cody, R. J., Moralejo, C. and Allen, J. E.: Photodissociation of the hydroxyl radical (OH) at 157 nm, J. Chem. Phys., 95(4), 2491, doi:10.1063/1.460953, 1991.

Gyawali, M., Arnott, W. P., Zaveri, R. A., Song, C., Flowers, B., Dubey, M. K., Setyan, A., Zhang, Q., China, S., Mazzoleni, C., Gorkowski, K., Subramanian, R. and Moosmüller, H.: Evolution of multispectral aerosol absorption properties in a biogenically-influenced urban environment during the CARES campaign, Atmosphere (Basel)., 8(11), doi:10.3390/atmos8110217, 2017.

Hassan, T., Moosmüller, H. and Chung, C. E.: Coefficients of an analytical aerosol forcing equation determined with a Monte-Carlo radiation model, J. Quant. Spectrosc. Radiat. Transf., 164(164), 129–136, doi:10.1016/j.jqsrt.2015.05.015, 2015.

Hennigan, C. J., Miracolo, M. A., Engelhart, G. J., May, A. A., Presto, A. A., Lee, T., Sullivan, A. P., McMeeking, G. R., Coe, H., Wold, C. E., Hao, W.-M., Gilman, J. B., Kuster, W. C., de Gouw, J., Schichtel, B. A., Collett Jr., J. L., Kreidenweis, S. M. and Robinson, A. L.: Chemical and Physical Transformations of Organic Aerosol from the Photo-Oxidation of Open Biomass Burning Emissions in an Environmental Chamber, Atmos. Chem. Phys., 11(15), 7669–7686, 2011.

IPCC, Stocker, T. F., Qin, D., Plattner, G.-K., Tignor, M., Allen, S. K., Boschung, J., Nauels, A., Xia, Y., Bex, V. and Midgley, P. M.: Climate Change 2013: The Physical Science Basis. Contribution of Working Group I to the Fifth Assessment Report of the Intergovernmental Panel on Climate Change, Cambridge University Press, Cambridge, United Kingdom and New York, USA., 2013.

Jolleys, M. D., Coe, H., McFiggans, G., Taylor, J. W., O'Shea, S. J., Le Breton, M., Bauguitte, S. J. B., Moller, S., Di Carlo, P., Aruffo, E., Palmer, P. I., Lee, J. D., Percival, C. J. and Gallagher, M. W.: Properties and Evolution of Biomass Burning Organic Aerosol from Canadian Boreal Forest Fires, Atmos. Chem. Phys., 15(6), 3077–3095, doi:10.5194/acp-15-3077-2015, 2015.

Lambe, A. T., Ahern, A. T., Williams, L. R., Slowik, J. G., Wong, J. P. S., Abbatt, J. P. D., Brune, W. H., Ng, N. L., Wright, J. P., Croasdale, D. R., Worsnop, D. R., Davidovits, P. and Onasch, T. B.: Characterization of aerosol photooxidation flow reactors: Heterogeneous oxidation, secondary organic aerosol formation and cloud condensation nuclei activity measurements, Atmos. Meas. Tech., doi:10.5194/amt-4-445-2011, 2011.

Levin, E. J. T., McMeeking, G. R., Carrico, C. M., Mack, L. E., Kreidenweis, S. M., Wold, C. E., Moosmüller, H., Arnott, W. P., Hao, W. M., J. L. Collett, J. and Malm, W. C.: Biomass Burning Smoke Aerosol Properties Measured during FLAME, J. Geophys. Res., 115(D18210), doi:10.1029/2009JD013601, 2010.

Lewis, K., Arnott, W. P. and Moosmüller, H.: Strong Spectral Variation of Biomass Smoke Light

Absorption and Single Scattering Albedo Observed with a Novel Dual-Wavelength Photoacoustic Instrument, J. Geophys. Res., 113(D16203), doi:10.1029/2007JD009699, 2008.

Liousse, C., Devaux, C., Dulac, F. and Cachier, H.: Aging of Savanna Biomass Burning Aerosols: Consequences on their Optical Properties, J. Atmos. Chem., 22(1–2), 1–17, 1995.

Mishchenko, M. I., Dlugach, J. M. and Liu, L.: Linear Depolarization of Lidar Returns by Aged Smoke Particles, Appl. Opt., 55(35), 9968–9973, doi:10.1364/AO.55.009968, 2016.

Moosmüller, H., Engelbrecht, J. P., Skiba, M., Frey, G., Chakrabarty, R. K. and Arnott, W. P.: Single scattering albedo of fine mineral dust aerosols controlled by iron concentration, J. Geophys. Res. Atmos., 117(11), 1–10, doi:10.1029/2011JD016909, 2012.

Moosmüller, H. and Arnott, W. P.: Angular truncation errors in integrating nephelometry, Rev. Sci. Instrum., 74(7), 3492–3501, doi:10.1063/1.1581355, 2003.

Moosmüller, H. and Arnott, W. P.: Particle optics in the rayleigh regime, J. Air Waste Manag. Assoc., 59(9), 1028–1031, doi:10.3155/1047-3289.59.9.1028, 2009.

Moosmüller, H. and Chakrabarty, R. K.: Technical Note: Simple analytical relationships between Ångström coefficients of aerosol extinction, scattering, absorption, and single scattering albedo, Atmos. Chem. Phys., 11(20), 10677–10680, doi:10.5194/acp-11-10677-2011, 2011.

Moosmüller, H. and Sorensen, C. M.: Small and large particle limits of single scattering albedo for homogeneous, spherical particles, J. Quant. Spectrosc. Radiat. Transf., 204, 250–255, doi:10.1016/j.jqsrt.2017.09.029, 2018.

Moosmüller, H., Chakrabarty, R. K. and Arnott, W. P.: Aerosol light absorption and its measurement: A review, J. Quant. Spectrosc. Radiat. Transf., doi:10.1016/j.jqsrt.2009.02.035, 2009a.

Moosmüller, H., Chakrabarty, R. K. and Arnott, W. P.: Aerosol light absorption and its measurement: A review, J. Quant. Spectrosc. Radiat. Transf., 110(11), 844–878, doi:10.1016/j.jqsrt.2009.02.035, 2009b.

Moosmüller, H., Chakrabarty, R. K., Ehlers, K. M. and Arnott, W. P.: Absorption Ångström coefficient, brown carbon, and aerosols: Basic concepts, bulk matter, and spherical particles, Atmos. Chem. Phys., 11(3), 1217–1225, doi:10.5194/acp-11-1217-2011, 2011.

Niyogi, D., Chang, H.-I., Saxena, V. K., Holt, T., Alapaty, K., Booker, F., Chen, F., Davis, K. J., Holben, B., Matsui, T., Meyers, T., Oechel, W. C., Pielke Sr., R. A., Wells, R., Wilson, K. and Xue, Y.: Direct Observations of the Effects of Aerosol Loading on Net Ecosystem C02 Exchanges over Different Landscapes, Geophys. Res. Lett., 31(L20506), DOI:10.1029/2004GLO20915, 2004.

Ortega, A. M., Day, D. A., Cubison, M. J., Brune, W. H., Bon, D., de Gouw, J. A. and Jimenez, J. L.: Secondary Organic Aerosol Formation and Primary Organic Aerosol Oxidation from Biomass-Burning Smoke in a Flow Reactor during FLAME-3, Atmos. Chem. Phys., 13(22), 11551–11571, doi:10.5194/acp-13-11551-2013, 2013.

Pokhrel, R. P., Wagner, N. L., Langridge, J. M., Lack, D. A., Jayarathne, T., Stone, E. A., Stockwell, C. E., Yokelson, R. J. and Murphy, S. M.: Parameterization of single-scattering albedo (SSA) and absorption Angstrom exponent (AAE) with EC/OC for aerosol emissions from biomass burning, Atmos. Chem. Phys., 16(15), doi:10.5194/acp-16-9549-2016, 2016.

Pope III, C. A. and Dockery, D. W.: Health Effects of Fine Particulate Air Pollution: Lines that Connect, J. Air Waste Manage. Assoc., 56(6), 709–742, 2006.

Popovicheva, O. B., Kozlov, V. S., Rakhimov, R. F., Shmargunov, V. P., Kireeva, E. D., Persiantseva, N. M., Timofeev, M. A., Engling, G., Eleftheriadis, K., Diapouli, E., Panchenko, M. V, Zimmermann, R. and Schnelle-Kreis, J.: Optical-Microphysical and Physical-Chemical Characteristics of Siberian Biomass Burning: Experiments in Aerosol Chamber, Atmos. Ocean. Opt., 29(6), 492–500, doi:10.1134/S1024856016060129, 2016.

Radke, L. F., Hegg, A. S., Hobbs, P. V and Penner, J. E.: Effects of Aging on the Smoke from a Large Forest-Fire, Atmos. Res., 38(1–4), 315–332, 1995.

Saleh, R., Hennigan, C. J., McMeeking, G. R., Chuang, W. K., Robinson, E. S., Coe, H., Donahue, N. M. and Robinson, A. L.: Absorptivity of Brown Carbon in Fresh and Photo-Chemically Aged Biomass-Burning Emissions, Atmos. Chem. Phys., 13(15), 7683–7693, doi:10.5194/acp-13-7683-2013, 2013.

Samburova, V., Connolly, J., Gyawali, M., Yatavelli, R. L. N., Watts, A. C., Chakrabarty, R. K., Zielinska, B., Moosmüller, H. and Khlystov, A.: Polycyclic Aromatic Hydrocarbons in Biomass-Burning Emissions and Their Contribution to Light Absorption and Aerosol Toxicity, Sci. Total Environ., 568, 391–401, doi:http://dx.doi.org/10.1016/j.scitotenv.2016.06.026, 2016.

Sengupta, D., Samburova, V., Bhattarai, C., Kirillova, E., Mazzoleni, L., Iaukea-Lum, M., Watts, A., Moosmüller, H. and Khlystov, A.: Light absorption by polar and non-polar aerosol compounds from laboratory biomass combustion, Atmos. Chem. Phys., 18(15), 10849–10867, doi:10.5194/acp-18-10849-2018, 2018.

Srinivas, B. and Sarin, M. M.: Brown carbon in atmospheric outflow from the Indo-Gangetic Plain: Mass absorption efficiency and temporal variability, Atmos. Environ., 89, 835–843, doi:10.1016/j.atmosenv.2014.03.030, 2014.

Sumlin, B. J., Heinson, W. R. and Chakrabarty, R. K.: Retrieving the aerosol complex refractive index using PyMieScatt: A Mie computational package with visualization capabilities, J. Quant. Spectrosc. Radiat. Transf., 205, 127–134, doi:10.1016/j.jqsrt.2017.10.012, 2018a.

Sumlin, B. J., Heinson, Y. W., Shetty, N., Pandey, A., Pattison, R. S., Baker, S., Hao, W. M. and Chakrabarty, R. K.: UV–Vis–IR spectral complex refractive indices and optical properties of brown carbon aerosol from biomass burning, J. Quant. Spectrosc. Radiat. Transf., 206, 392–398, doi:10.1016/j.jqsrt.2017.12.009, 2018b.

Taylor, J. R.: An introduction to error analysis, Second., edited by A. McGuire, University Science Books, Sausalito, CA., 1997.

Tie, X., Huang, R.-J., Dai, W., Cao, J., Long, X., Su, X., Zhao, S., Wang, Q. and Li, G.: Effect of Heavy Haze and Aerosol Pollution on Rice and Wheat Productions in China, Sci. Rep., 6, 29612, doi:10.1038/srep29612, 2016.

TSI INC: Product Information: Electrostatic Classifiers (Model 3080). [online] Available from: dustmonitors.ru/d/68562/d/1933792g-3080.pdf, 2001.

Turetsky, M. R., Benscoter, B., Page, S., Rein, G., Van Der Werf, G. R. and Watts, A.: Global vulnerability of peatlands to fire and carbon loss, Nat. Geosci., 8(1), 11–14, doi:10.1038/ngeo2325, 2015.

Watson, J. G.: 2002 Critical Review -- Visibility: Science and Regulation, J. Air Waste Manage. Assoc., 52(6), 626–713, 2002.

Yu, Z., Beilman, D. W., Frolking, S., MacDonald, G. M., Roulet, N. T., Camill, P. and Charman, D. J.: Peatlands and Their Role in the Global Carbon Cycle, Eos, Trans. Am. Geophys. Union, 92(12), 97, doi:10.1029/2011EO120001, 2011.

Yu, Z., Assif, J., Magoon, G., Kebabian, P., Brown, W., Rundgren, W., Peck, J., Miake-Lye, R., Liscinsky, D. and True, B.: Differential photoacoustic spectroscopic (DPAS)-based technique for PM optical absorption measurements in the presence of light absorbing gaseous species, Aerosol Sci. Technol., 51(12), 1438–1447, doi:10.1080/02786826.2017.1363866, 2017.

Yu, Z. C.: Northern peatland carbon stocks and dynamics: A review, Biogeosciences, 9(10), 4071–4085, doi:10.5194/bg-9-4071-2012, 2012.